

## Stress Analysis of Muzzle Brake by Using Fluid-Solid Coupled Method

Hong-xia Lei, Zhi-jun Wang and Jun-li Zhao

<sup>1</sup>College of Mechatronic Engineering, North University of China, Taiyuan, 030051, China

Received 28 April 2016; Accepted 12 September 2016

### Abstract

Although muzzle brake is an important device for guns, its working environment is poor. Originally, muzzle brake was designed to be very large and bulky to satisfy the strength requirement, which caused increase in material resources and weight. Therefore, a new method should be developed for muzzle brake design. In this study, the stress analysis of muzzle brake was made by using finite element analysis based on fluid-solid coupled method to evaluate muzzle brake's reliability. First, a 3D computational domain was constructed to simulate the muzzle flow field, and the Spalart-Allmaras model was utilized for turbulent flow calculation. Second, muzzle brake force was examined in details in the gun firing process, and the figures of pressure distribution on muzzle brake surfaces were obtained. Finally, a loosely fluid-solid coupled method was employed to calculate the stress of the muzzle brake. Results show that the maximum stress is 624.71 MPa, which satisfies the strength requirement. The holes and baffles of each row have different stress values. Compared with that of the other rows along the flow direction, the maximum stress values of the holes and baffles of the second and third rows are larger. What's more, those of the fourth to the sixth rows decrease gradually. The maximum stress points of each row appear at the junction of the holes and the baffles. Thus, this study is meaningful and significant for the design and optimization of muzzle brake.

*Keywords:* Muzzle brake, Muzzle flow field, Fluid-solid coupled method, Dynamic mesh, Unsteady flow.

### 1. Introduction

In the process of gun firing, a projectile is pushed by the explosion of propellant inside gun tube. When the projectile is flying out through a muzzle brake, high-temperature and high-pressure propellant gas is suddenly released through the muzzle brake. The gas expands rapidly at a high speed. At the same time, a complex high-pressure blast flow field is generated, which is actually a complex 3D unsteady problem. With the flow field around the muzzle brake changing constantly, the muzzle brake force is also continuously changing all the time. In addition, the muzzle blast wave greatly affects the surfaces of the muzzle brake. So many factors need to be taken into consideration in the process of muzzle brake designing. However, there are few defects in the traditional design of muzzle brake. At the theoretical calculation stage, the load applied on the surfaces of muzzle brake is based on experience. Thus, to some degree, this approach is subjective and limited. What's more, although the component satisfies the stress requirement, the disadvantages of material-wasting and weight-increasing are unavoidable. At the testing verification stage, the parameters of muzzle brake are determined through conducting several actual firing tests to check the bearing capacity of muzzle brake. To a certain extent, such an approach is uneconomical in terms of money, manpower, and material resources. The load produced by muzzle flow on muzzle brake is complex and constantly changing. Therefore, accurate calculation of muzzle brake force, pressure distribution on the surfaces of muzzle brake and stress analysis of muzzle brake are

primary to the design of muzzle brake. They are the focuses of the current related research. A growing number of researchers are now exploring ways of reducing the weight of muzzle brake without altering its performance.

### 2. State of The Art

With the development of computational fluid dynamics (CFD) technology and the improved performance of computer in recent years, CFD methods have been increasingly used to guide muzzle brake design. Domestic and foreign scholars have utilized various methods to study the flow field, especially the structure of muzzle blast flow. Zonglin Jiang solved Euler equations by using a dispersion-controlled scheme implemented with moving boundary conditions [1]. Xiao-hai Jiang et al. applied the AUSMDV scheme to solve Euler equations and the dynamic chimera grid technique to simulate the flow field of the launching process with a moving projectile in a nearly realistic situation [2]. Zhang Huan-hao et al. simulated the flying away of a high-speed projectile from the bores through different muzzle brakes by using a high-resolution Roe scheme and the structured dynamic mesh techniques based on the 2D unsteady Euler equation [3]. The sound pressure surrounding muzzle device has also been studied by many researchers. Kuk-Jeong Kang et al. investigated the impulsive sound attenuation for a high-pressure blast flow field. In their study, the pressure variation of the blast flow field was analyzed to evaluate the effect of a silencer [4]. Hafizur Rehman et al. employed a large-caliber 120 mm K1A1 tank gun to analyze the high-pressure impulsive sound generated during the blast flow [5]. Jonghoon Bin et

\* E-mail address: Leihongxia@nuc.edu.cn

al. studied the impulsive noise produced by complex flows discharging from a muzzle and analyzed the basic structures that generate impulsive noise [6]. Guo Ze-qing et al. studied the effects of the precursor flow on the muzzle propellant flow field [7]. A. Merlen and A. Dymont applied ultra-high-speed visualization to observe the flow that follows the discharge of firearms [8]. M M Biss et al. studied the shadowgraphy of shock waves from explosions and gunshots in large fields-of-view [9].

However, all of these studies are focused on the structure of the flow field and the pressure produced by the muzzle blast around different muzzles. The effect of the complex muzzle flow on muzzle brake has not been reported in the corresponding literature. This research gap can be bridged by fluid-solid coupled numerical simulation. Grétarsson et al. considered the numerically stable fluid-structure interactions between compressible flow and solid structures [10]. Wang et al. established computational algorithms for tracking dynamic fluid-structure interfaces embedded in boundary methods [11]. This method has been applied in many fields, such as the flood flow in arteries, the fluid flow in pipelines, and the fluid-structure interaction analysis of compressor blades [12], [13], [14], [15]. The results prove that this technique obtains calculation results that are close to the actual working conditions, and it provides a higher accuracy theory for designing of the structure.

The main purpose of the study is to conduct numerical simulations based on CFD technology and loosely fluid-solid coupled method to analyze the force and stress of muzzle brake. The flow field of a muzzle brake was simulated, and the force produced by every row of side holes and baffles was then analyzed. Then the stress of the muzzle brake was studied by loading the gas force on the corresponding surfaces of the muzzle brake. The results of this study provide some reference to the structural optimization of muzzle brake.

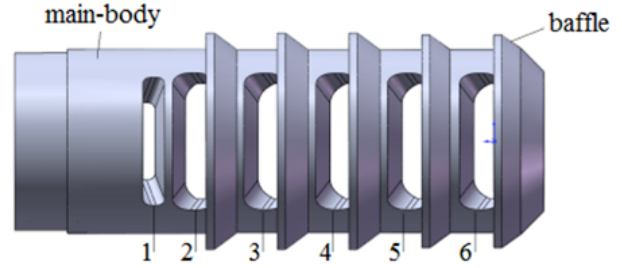
### 3. Methodology

#### 3.1 Muzzle brake model

The muzzle brake structure in this paper is shown in Fig. 1. As shown, the model is made up of a main-body and many baffles. There are six rows of holes on the main-body, and the side holes of each row are symmetrical. Propellant gas sprays from the holes from the first to the sixth row in proper sequence. The two side holes of the first row are inclined to the front to reduce the impact of high-pressured and high-temperated propellant gas on the rear side of the muzzle brake by changing the direction of the propellant gas through the other side holes, while the lateral holes of the other five rows are inclined to the rear mainly to reduce the recoil force.



(a) the material object of the muzzle brake



(b) the established model

Fig. 1 Schematic diagram of the muzzle brake

#### 3.2 Fluid Mathematical Model

To simulate the complex flow through the muzzle brake, 3D N-S equations are used for the governing equations. Chemical reactions are assumed to have an insignificant effect on the flow. The equation can be expressed as follows:

$$\frac{\partial U}{\partial t} + \frac{\partial F}{\partial x} + \frac{\partial G}{\partial y} + \frac{\partial H}{\partial z} = \frac{\partial F_1}{\partial x} + \frac{\partial G_1}{\partial y} + \frac{\partial H_1}{\partial z} \quad (1)$$

where  $U$  is the variable to be solved,  $F, G,$  and  $H$  are the inviscid fluxes in three coordinate directions,  $F_1, G_1,$  and  $H_1$  are the viscid fluxes in three coordinate directions,  $U, F, G, H, F_1, G_1,$  and  $H_1$  are defined, respectively, as follows:

$$U = [\rho \quad \rho u \quad \rho v \quad \rho w \quad e]^T,$$

$$F = [\rho u \quad \rho u^2 + p \quad \rho uv \quad \rho wu \quad (e+p)u]^T,$$

$$G = [\rho v \quad \rho uv \quad \rho v^2 + p \quad \rho vw \quad (e+p)v]^T,$$

$$H = [\rho w \quad \rho wu \quad \rho vw \quad \rho w^2 + p \quad (e+p)w]^T,$$

$$F_1 = [0 \quad \tau_{xx} \quad \tau_{xy} \quad \tau_{xz} \quad u\tau_{xx} + v\tau_{xy} + w\tau_{xz} - q_x]^T,$$

$$G_1 = [0 \quad \tau_{yx} \quad \tau_{yy} \quad \tau_{yz} \quad u\tau_{yx} + v\tau_{yy} + w\tau_{yz} - q_y]^T,$$

$$H_1 = [0 \quad \tau_{zx} \quad \tau_{zy} \quad \tau_{zz} \quad u\tau_{zx} + v\tau_{zy} + w\tau_{zz} - q_z]^T,$$

$$\tau_{xx} = \frac{2}{3}\mu \left( 2\frac{\partial u}{\partial x} - \frac{\partial v}{\partial y} - \frac{\partial w}{\partial z} \right), \quad \tau_{xy} = \tau_{yx} = \mu \left( \frac{\partial u}{\partial y} + \frac{\partial v}{\partial x} \right),$$

$$\tau_{yy} = \frac{2}{3}\mu \left( 2\frac{\partial v}{\partial y} - \frac{\partial u}{\partial x} - \frac{\partial w}{\partial z} \right), \quad \tau_{xz} = \tau_{zx} = \mu \left( \frac{\partial w}{\partial x} + \frac{\partial u}{\partial z} \right),$$

$$\tau_{zz} = \frac{2}{3}\mu \left( 2\frac{\partial w}{\partial z} - \frac{\partial u}{\partial x} - \frac{\partial v}{\partial y} \right), \quad \tau_{yz} = \tau_{zy} = \mu \left( \frac{\partial v}{\partial z} + \frac{\partial w}{\partial y} \right),$$

$$q_x = -k \frac{\partial T}{\partial x}, \quad q_y = -k \frac{\partial T}{\partial y}, \quad q_z = -k \frac{\partial T}{\partial z},$$

where  $\rho$  is density,  $u$ ,  $v$ , and  $w$  are Cartesian velocity components for the  $x$ ,  $y$  and  $z$  directions, respectively,  $p$  is the pressure,  $k$  is the conductivity of the gas,  $\tau_{ij}$  represents the viscous stresses, and  $e$  is the total energy per unit volume, which is defined as

$$e = \frac{p}{\gamma - 1} + \frac{1}{2} \rho (u^2 + v^2 + w^2). \quad (2)$$

Parameter  $\gamma$  denotes the specific heat ratio. The ideal-gas equation of state is defined as

$$p = \rho RT. \quad (3)$$

The Prandtl Number is expressed as

$$Pr = \frac{c_p}{k} \mu \approx 0.72, \quad (4)$$

and  $\mu$  is given by

$$\mu = C_1 \frac{T^{3/2}}{T + C_2}. \quad (5)$$

Eqs. (1) to (5) constitute a closed system of equations.

### 3.3 Solid Mathematical Model

The stress formula  $\sigma_{ij} = \lim_{\Delta A_i \rightarrow 0} \left( \frac{\Delta F_i}{\Delta A_i} \right)$ , in which  $\Delta F_i$  is the force in  $i$  direction and  $\Delta A_i$  is the stress area in the  $i$  direction.

The force balance equation:

$$\begin{cases} \frac{\partial \sigma_x}{\partial x} + \frac{\partial \tau_{yx}}{\partial y} + \frac{\partial \tau_{zx}}{\partial z} + F_x = 0 \\ \frac{\partial \tau_{xy}}{\partial x} + \frac{\partial \sigma_y}{\partial y} + \frac{\partial \tau_{zy}}{\partial z} + F_y = 0, \\ \frac{\partial \tau_{xz}}{\partial x} + \frac{\partial \tau_{yz}}{\partial y} + \frac{\partial \sigma_z}{\partial z} + F_z = 0 \end{cases} \quad (6)$$

where  $\sigma_x, \sigma_y, \sigma_z$  are stress components,

$\tau_{xy}, \tau_{xz}, \tau_{yx}, \tau_{yz}, \tau_{zx}, \tau_{zy}$  are shear stress components, and  $F_x, F_y$ , and  $F_z$  are the volume forces on the three coordinate axes.

The equation of strain compatibility is

$$\begin{cases} \epsilon_x = \frac{\partial u}{\partial x} \\ \epsilon_y = \frac{\partial v}{\partial y} \\ \epsilon_z = \frac{\partial w}{\partial z} \\ \gamma_{xy} = \gamma_{yx} = \frac{\partial v}{\partial x} + \frac{\partial u}{\partial y} \\ \gamma_{yz} = \gamma_{zy} = \frac{\partial w}{\partial y} + \frac{\partial v}{\partial z} \\ \gamma_{zx} = \gamma_{xz} = \frac{\partial u}{\partial z} + \frac{\partial w}{\partial x} \end{cases} \quad (7)$$

where  $\epsilon_x, \epsilon_y, \epsilon_z$  are strain components, and

$\gamma_{xy}, \gamma_{xz}, \gamma_{yx}, \gamma_{yz}, \gamma_{zx}, \gamma_{zy}$  are shear strain components.

The constitutive equation is

$$\begin{cases} \epsilon_x = \frac{1}{E} [\sigma_x - \nu(\sigma_y + \sigma_z)] \\ \epsilon_y = \frac{1}{E} [\sigma_y - \nu(\sigma_x + \sigma_z)] \\ \epsilon_z = \frac{1}{E} [\sigma_z - \nu(\sigma_x + \sigma_y)] \\ \gamma_{xy} = \frac{2(1+\nu)}{E} \tau_{xy} \\ \gamma_{yz} = \frac{2(1+\nu)}{E} \tau_{yz} \\ \gamma_{xz} = \frac{2(1+\nu)}{E} \tau_{xz} \end{cases}, \quad (8)$$

where  $E$  and  $\nu$  respectively represent the elastic modulus and Poisson's ratio.

### 3.4 Turbulence Model

The Spalart-Allmaras model is applied for turbulent flow calculation. It includes a developed single-equation model and is effective for simulating boundary layer flow fields for adverse pressure gradient problems. The transport equation for turbulent energy of the Spalart-Allmaras model is expressed as follows:

$$\begin{aligned} \frac{\partial(\rho k)}{\partial t} + \frac{\partial(\rho k u_i)}{\partial x_i} = \frac{\partial}{\partial x_j} \left[ \left( \mu + \frac{u_i}{\sigma_k} \right) \frac{\partial k}{\partial x_j} \right] + \\ + \mu_t \left( \frac{\partial u_i}{\partial x_j} + \frac{\partial u_j}{\partial x_i} \right) \frac{\partial u_i}{\partial x_j} - \rho C_D \frac{k^{\frac{3}{2}}}{l} \end{aligned} \quad (9)$$

From left to right, the terms represent transient, advection, diffusion, generation, and dissipation effects, respectively. The turbulent viscosity is calculated by the following Kolmogorov-Prandtl expression

$$\mu_t = \rho C_\mu \sqrt{k} l, \quad (10)$$

$\sigma_k, C_D, C_\mu$  are empirical coefficients.

### 3.5 Initial and Boundary Conditions

Initial conditions include velocity, pressure, density, temperature, etc. In the internal ballistics period, the friction between the projectile and the tube is assumed negligible, and the driving force acting on the projectile can sufficiently overcome the friction and the drag force to keep the projectile moving inside the tube. When the projectile begins to move out of the tube, the motion of the projectile obeys Newton's law. The loading conditions include the pressure, velocity, and temperature of the propellant gas in the tube. All the distribution of parameters can be obtained by solving the internal ballistics.

The boundary conditions used in this simulation include plane symmetric boundary, moving boundary, wall boundary, and pressure outlet boundary. Plane symmetric boundary and pressure outlet boundary are shown in Fig. 2.

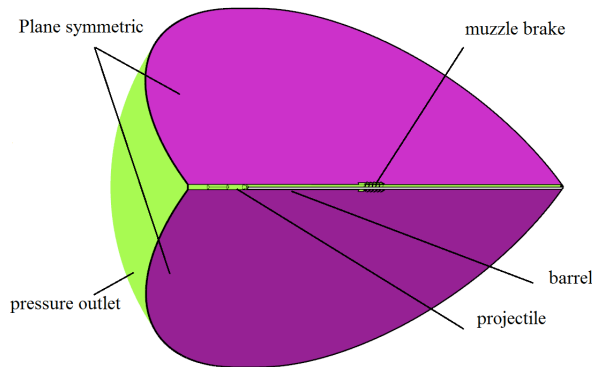


Fig. 2 Boundary conditions

### 3.6 Fluid-solid Coupled Mathematical Model

In the gun firing process, the muzzle brake has a remarkable influence on the flow field. By contrast, the deformation caused by fluid flow on the muzzle is insignificant. Therefore, one-way fluid-solid coupled method is used in this study. The geometrical compatibility conditions and the equilibrium conditions on the coupled interface must be satisfied. In this study, the boundary conditions applied on the fluid-solid coupled interface are as follows:

$$\tau^f \cdot n_f \Big|_{\Gamma} = \tau^s \cdot n_s \Big|_{\Gamma}, \quad (11)$$

where  $M$  is the fluid-solid coupled interface, the superscript  $f$  and  $s$  represent the values associated with the fluid and solid, respectively,  $n$  is the unit outward normal of fluid and solid sub-domain, and  $\tau$  is the stress. In the equilibrium conditions, the action of the shear force applied on the fluid-solid coupled interface by the gas flow is neglected because this shear force is smaller than the pressure force.

## 4. Simulation Analysis and Discussion

### 4.1 Method validation with experiments

To verify the correctness of the calculation, the efficiency of muzzle brake is calculated by using the efficiency calculating formula, which can be expressed as

$$\eta = \frac{E_0 - E_1}{E_0} \times 100\% = \frac{M_0 W_{\max 0}^2 - M_1 W_{\max 1}^2}{M_0 W_{\max 0}^2} \times 100\% \quad (12)$$

where the subscript label 0 and 1 represent without and with the muzzle brake.  $M$  is the quality of recoiling parts and  $W$  is

the free recoil velocity of the tube at the start of the aftereffect period.

Computational results reveal that the efficiency of the muzzle brake is 44.08%, which is close to the experimental efficiency (43%). The error is 2.5%, suggesting that the calculation assumptions based on the unsteady flow and the calculation method are correct.

### 4.2 Muzzle brake force analysis

Fig. 3 shows the force history of the muzzle brake. Fig. 3(a) presents that the precursor flow has an insignificant effect on the muzzle brake in the interior ballistic period. Meanwhile, Fig. 3(b) illustrates that the muzzle brake force rises rapidly within 1 ms. At the beginning of the aftereffect period, the high-pressured propellant gas begins to flow out the side holes of the first row first, at point A. The pressure acting on the side holes provides force to the muzzle brake, causing the force curve generate the first rise approaching point B. Then, the high-pressured gas expands into the chamber, which is located before the holes in the second row, and acts on the surfaces of the side holes and their baffles of the second row. After that, the muzzle brake force curve rises rapidly until point C. Following that, the propellant gas spreads to next chamber and produces recoil force firstly and muzzle brake force secondly. The CD curve shows the changing process of the force. Next, the propellant gas passes through the following chambers in the same way. When the propellant gas flows out of the muzzle brake, recoil force is produced by the pressure acting on the surface wall at the front end of the muzzle brake, and the muzzle brake force is reduced gradually.

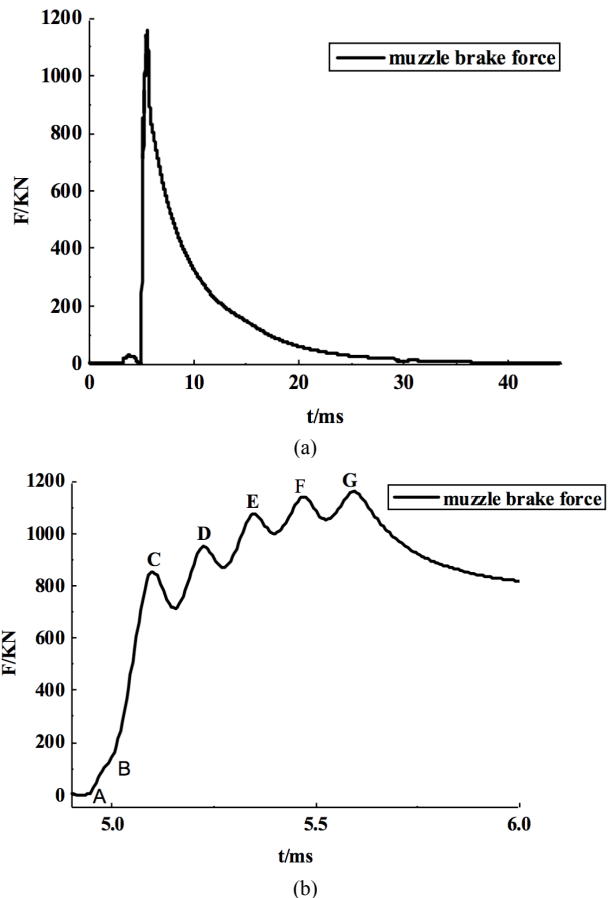


Fig. 3 Force history of the muzzle brake

Fig. 4 shows the force history of the holes and their baffles of each row. In Fig. 4(a), in the bore movement

period, when the projectile is close to the muzzle brake, the muzzle brake force is relatively small. The reason is that no propellant gas is being ejected, and only the precursor flow affects the holes and their baffles of each row. In Fig. 4(b), in the aftereffect period, although all side holes and their baffles have the same structure, except for the holes of the first row, the maximum force values produced by the holes and their baffles of each row do not appear at the same time and change from 706.72 KN to 274.83 KN. The numerical values differ greatly. This characteristic suggests the possibility of improving the efficiency of muzzle brakes. The muzzle brake force should be improved by changing the distance between the holes of each row to ensure the maximum force values to be approximately equal to one another. In addition, the analysis method based on the flow field provides a new way to calculate the efficiency of muzzle brakes.

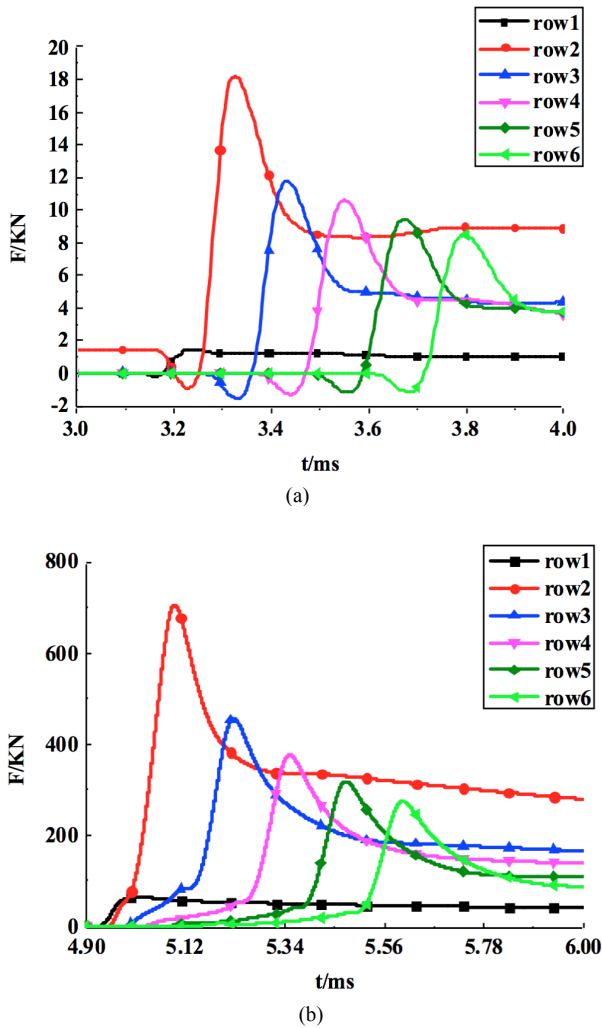


Fig. 4 Force history of each row of holes and their baffles

**4.3 Analysis of the average pressure on the main surfaces of the muzzle brake**

The muzzle brake structure is very complex. The side holes and baffles are the main bearing parts. To acquire the realistic and detailed stress status of the muzzle brake in the firing process, a half model of the muzzle brake is established to number sixty-one bearing surfaces. Except the side holes of the first row, the other side holes and baffles share the same structure. There are three main bearing surfaces on two side holes of the first row, as for the rest, there are seven. Taking the holes of the second row as an example, the main bearing surfaces are shown in Fig. 5.  $S_{ij}$

represents the main bearing surfaces, where  $i$  in subscript 1 indicates the number of holes and baffles in the direction of the flowing propellant gas, and  $j$  in subscript 2 represents the surfaces with different colors.

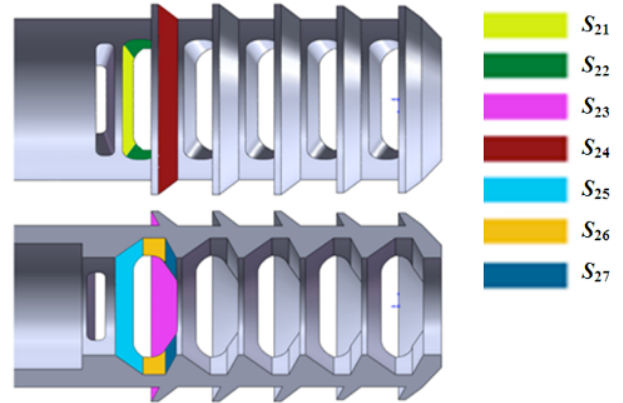
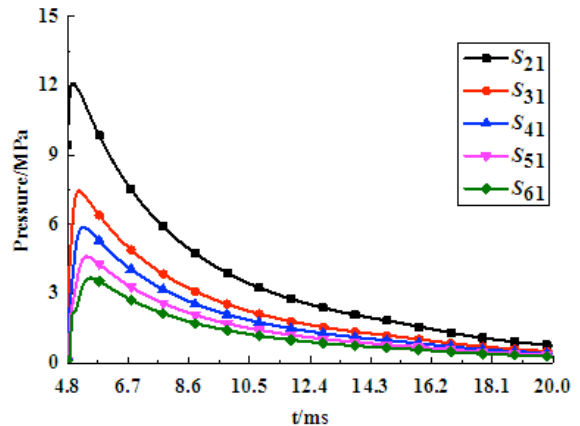


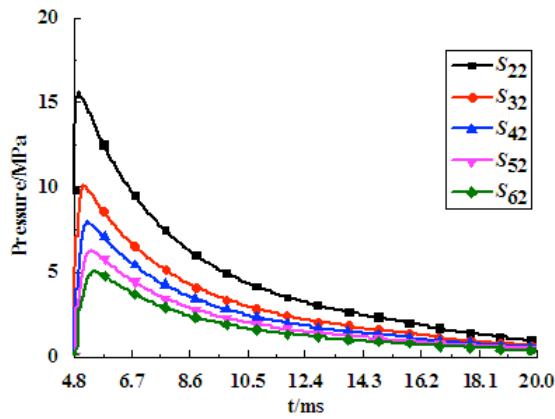
Fig. 5 Main bearing surfaces of the muzzle brake

In the firing process, when the projectile is passing through the muzzle brake, there is a strong impact on the various surfaces of the muzzle brake, and the pressure on every surface of the muzzle brake is constantly changing all the time. The variations of the average pressure values with the change of time on the surfaces of the holes with the same structure are compared. In the interior ballistic period, the effect on the muzzle brake produced by the precursor flow is small; as such, the time in the following analysis is recorded from the starting time of the aftereffect period. Fig. 6 shows the curves of the average pressure on the surfaces with the same structure over time. As shown in the figure, the maximum pressure values appear on the inner faces of every chamber, the average pressure values on the surfaces with the same structure achieve their maximum values in the direction of the gun launch, and the maximum values differ from one another.

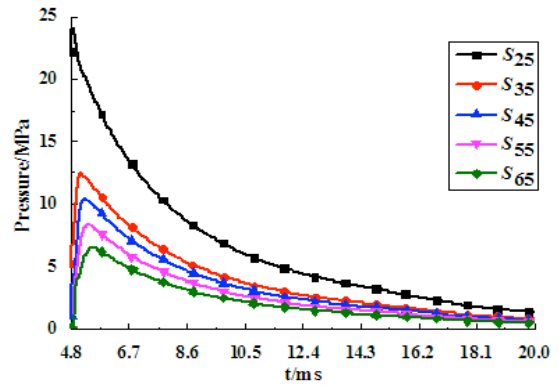
The maximum pressure values and the corresponding time for the main bearing surfaces are shown in Table 1, which shows that the maximum pressure value on muzzle brake can reach up to 37.4 Mpa. These results indicate that the surface pressure is one of the key factor in the design of muzzle brake. This value can also serve as an important reference for the study of muzzle blast wave.



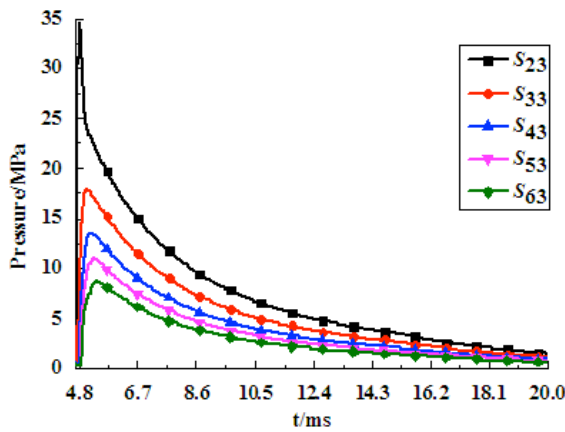
(a) Average pressure on the  $S_{1i}$  surfaces



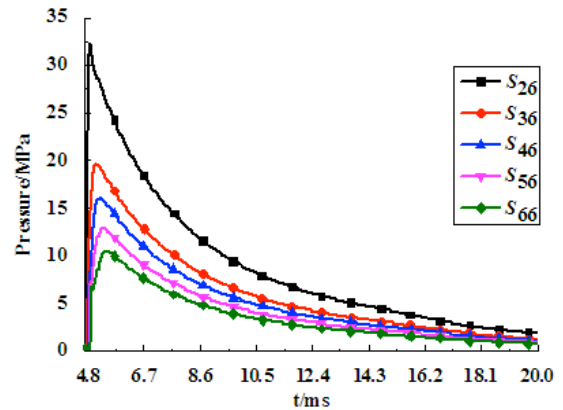
(b) Average pressure on the  $S_{12}$  surfaces



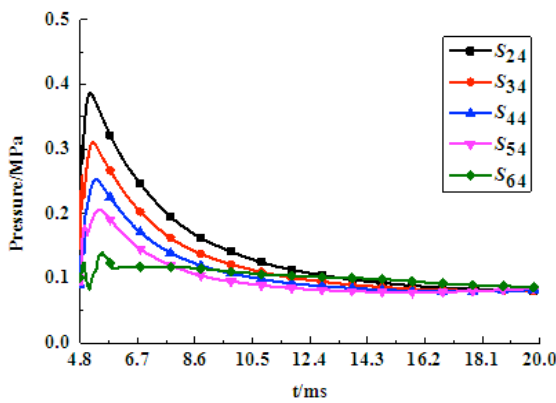
(e) Average pressure on the  $S_{15}$  surfaces



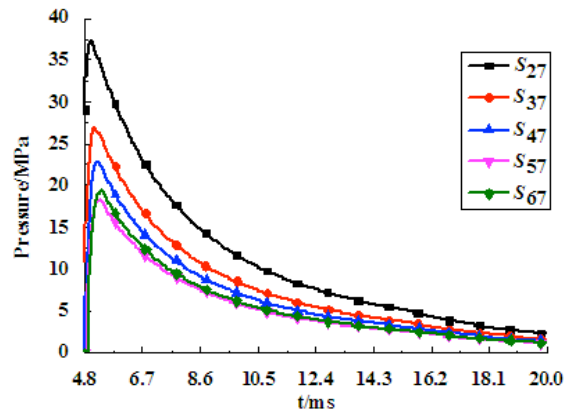
(c) Average pressure on the  $S_{13}$  surfaces



(f) Average pressure on the  $S_{16}$  surfaces



(d) Average pressure on the  $S_{14}$  surfaces



(g) Average pressure on the  $S_{17}$  surfaces

Fig. 6 Average pressure curves of the main bearing surfaces with the same structure

Table 1 Maximum pressure values and the corresponding time for the main bearing surfaces

| Surface  | Time/ms | max pressure/Mpa | Surface  | Time/ms | max pressure/Mpa |
|----------|---------|------------------|----------|---------|------------------|
| $S_{11}$ | 4.95    | 13.36            | $S_{34}$ | 5.21    | 0.31             |
| $S_{12}$ | 4.86    | 17.65            | $S_{44}$ | 5.31    | 0.253            |
| $S_{13}$ | 4.88    | 21.41            | $S_{54}$ | 5.43    | 0.206            |
| $S_{21}$ | 4.98    | 12.1             | $S_{64}$ | 5.52    | 0.141            |
| $S_{31}$ | 5.16    | 7.44             | $S_{25}$ | 4.85    | 24.1             |
| $S_{41}$ | 5.28    | 5.88             | $S_{35}$ | 5.12    | 12.4             |
| $S_{51}$ | 5.4     | 4.61             | $S_{45}$ | 5.24    | 10.41            |
| $S_{61}$ | 5.52    | 3.68             | $S_{55}$ | 5.37    | 8.35             |
| $S_{22}$ | 4.94    | 15.6             | $S_{65}$ | 5.48    | 6.53             |
| $S_{32}$ | 5.13    | 10.08            | $S_{26}$ | 4.87    | 32.25            |
| $S_{42}$ | 5.25    | 7.94             | $S_{36}$ | 5.09    | 19.71            |
| $S_{52}$ | 5.37    | 6.25             | $S_{46}$ | 5.2     | 16.12            |

|          |      |       |          |      |       |
|----------|------|-------|----------|------|-------|
| $S_{62}$ | 5.48 | 5.07  | $S_{56}$ | 5.31 | 12.91 |
| $S_{23}$ | 4.8  | 34.6  | $S_{66}$ | 5.44 | 10.44 |
| $S_{33}$ | 5.04 | 17.87 | $S_{27}$ | 5.0  | 37.4  |
| $S_{43}$ | 5.17 | 13.51 | $S_{37}$ | 5.12 | 26.93 |
| $S_{53}$ | 5.28 | 10.98 | $S_{47}$ | 5.21 | 22.8  |
| $S_{63}$ | 5.36 | 8.69  | $S_{57}$ | 5.28 | 18.3  |
| $S_{24}$ | 5.13 | 0.386 | $S_{67}$ | 5.34 | 19.5  |

#### 4.4 Muzzle brake stress analysis

In this work, one-flow fluid-solid coupled method is used to load the CFD calculation results on every surface of the muzzle brake at different time. The finite element method is employed to analyze the muzzle brake stress.

Fig. 7 depicts the stress distribution of the muzzle brake, which varies over time. The stress values are greater on the inner surfaces than those on the outer surfaces because the high-temperature and high-pressure propellant gas directly acts on the inner surfaces of the muzzle brake, and the pressure values on the inner surfaces are significantly higher than that on the outer surfaces. Although the holes and baffles from the second to the sixth rows have the same structure, the stress values of the holes of the second and third rows are relatively larger than those of other rows at any time. In addition, the maximum stress values of the same structure decrease from the second row to the sixth row. The maximum stress value is 624.71 Mpa, which is lower than the yield limit of the material (1200 MPa). Although the maximum stress satisfies the strength requirement, the material utilization rate remains low. The volume and weight of the muzzle brake can be reduced by changing the structure parameters, such as the baffles and the main body to attain structural optimization.

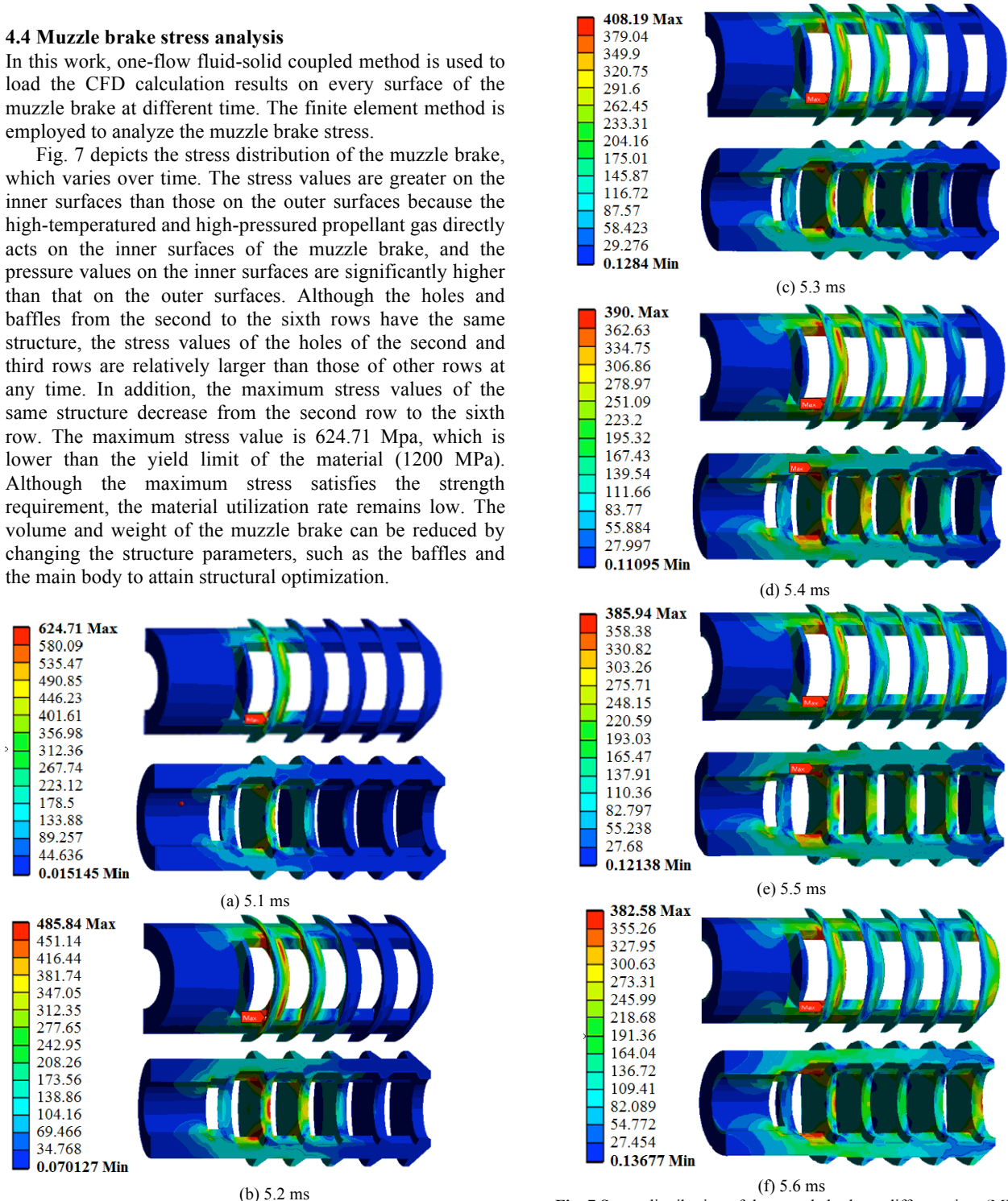


Fig. 7 Stress distribution of the muzzle brake at different time (MPa)

#### 5. Conclusion

In this work, numerical simulation of a muzzle brake flow based on CFD technology was conducted during the firing

process with a projectile. Then, the stress distribution of the muzzle brake at different time was analyzed by applying fluid-solid coupled method. The main conclusions are as follows:

(1) The muzzle brake efficiency value calculated by the numerical simulation was in good agreement with the experimental value. The method proposed in this study provides significant guidance for the performance analysis of muzzle brake design.

(2) The muzzle brake force provided by side holes and baffles of each row was analyzed in detail. The change of muzzle brake force with the change of time is consistent with the physical rule followed by high-temperature and high-pressure propellant gas. The analysis method can improve the efficiency of calculation in the design of muzzle brake.

(3) The stress distribution of the muzzle brake at different time was analyzed by using fluid-solid coupled method. The analysis method can be used for stress checks of different structures in bad environments, and it greatly reduces test costs.

The results of numerical simulation and analysis are helpful to the design of muzzle brake, particularly for the optimization of the structural parameters, such as wall thickness and weight. Nonetheless, this study is hindered by a number of limitations. The chemical reactions between the propellant gases were not considered in the analysis. The stress test was not verified because of the limitation of experiment condition. In future works, the simulation results should be verified by stress tests.

## References

- Zonglin Jiang, "Wave dynamic processes induced by a supersonic projectile discharging from a shock tube", *Physics of Fluids*, 15 (6), 2003, pp. 1665-1675.
- Xiaohai Jiang, Zhihua Chen, Baochun Fan, Hongzhi Li, "Numerical simulation of blast flow fields induced by a high-speed projectile", *Shock Waves*, 18, 2008, pp. 205-212.
- Zhang Huan-hao, Chen Zhi-hua, Jiang Xiao-hai, HAN Jun-li, "Investigation on the Blast Wave Structures of a High-speed projectile flying through different muzzle brakes", *Acta Armamentarii*, 33 (5), 2012, pp. 23-629.
- Kuk-Jeong Kang, Sung-Ho Ko and Dong-Soo Lee, "A study on impulsive sound attenuation for a high-pressure blast flow-field", *Journal of Mechanical Science and Technology* 22, 2008, pp. 190-200.
- Hafizur Rehman, Seung Hwa Hwang, Berkah Fajar, Hanshik Chung and Hyomin Jeong, "Analysis and attenuation of impulsive sound pressure in large caliber weapon during muzzle blast", *Journal of Mechanical Science and Technology*, 25 (10), 2011, pp. 2601-2606.
- Jonghoon Bin, Minwoo Kim, Soogab Lee, "A numerical study on the generation of impulsive noise by complex flows discharging from a muzzle", *International Journal for Numerical Methods in Engineering*, 75 (8), 2008, pp. 964-991.
- Guo Ze-qing, Wang Yang, Jiang Xiao-hai, Li Hong-zhi, "Numerical study on effects of precursor flow on muzzle propellant flow field", *Acta Armamentarii*, 33 (6), 2012, pp. 623-629.
- A. Merlen and A. Dymont, "Similarity and asymptotic analysis for gun-firing aerodynamics", *Journal of Fluid Mechanics*, 225, 1991, pp. 497-528.
- M.M. Biss, G.S. Settles, M.J. Hargather, L.J. Dodson, and J.D. Miller, "High-speed digital shadowgraphy of shock waves from explosions and gunshots", *Shock Waves*, (2), 2009, pp. 91-96.
- Grétarsson, J.T., Kwatra, N., Fedkiw, R., "Numerically stable fluid-structure interactions between compressible flow and solid structures", *Journal of Computational Physics*, 230 (8), 2011, pp. 3062-3084.
- Wang, K., Grétarsson, J., Main, A., Farhat, C., "Computational algorithms for tracking dynamic fluid-structure interfaces in embedded boundary methods", *International Journal for Numerical Methods in Fluids*, 70 (4), 2012, pp. 515-535.
- Liu-Chun, Bai Xiang-zhong, Li Xiao-bao, "Deformation and stress analysis of stenosed vessels", *Engineering Mechanics*, 30 (2), 2013, pp. 464-469.
- Kong Fan-yu, Chen Hao, Wang Ting, "Strength Analysis of Decompression Tower Bottom Pump's Pump Casing Based on Fluid-solid Coupling", *Journal of Mechanical Engineering*, 49 (2), 2013, pp. 159-164.
- Tao Hai-liang, Zhu Yang-li, Guo Bao-ting, Tan Chun-qing, "Numerical simulation of aeroelastic response in compressor based on fluid-structure coupling", *Journal of Aerospace Power*, 27 (5), 2012, pp. 1054-1060.
- Peng Guangjie, Wang Zhengwei, "Strength analysis of a large centrifugal dredge pump case", *Engineering Failure Analysis*, 16 (1), 2009, pp.321-328.